The Meteoritical Society

Meteoritics & Planetary Science 42, Nr 11, 1893–1903 (2007)
Abstract available online at http://meteoritics.org

Characteristics of oceanic impact-induced large water waves—Re-evaluation of the tsunami hazard

Kai WÜNNEMANN[1*], Robert WEISS[2], and Kay HOFMANN[1]

[1]Museum für Naturkunde, Humboldt Universität zu Berlin, Invalidenstrasse 43, 10115 Berlin, Germany
[2]Joint Institute for the Study of the Atmosphere and Ocean, University of Washington–National Center for Tsunami Research, Pacific Marine Environmental Laboratory, 7600 Sand Point Way Northeast, Seattle, Washington 98115, USA
*Corresponding author. E-mail: kai.wuennemann@museum.hu-berlin.de

(Received 02 November 2006; accepted 16 February 2007)

Abstract–The potential hazard of a meteorite impact in the ocean is controversial with respect to the destructive power of generated large ocean waves (tsunamis). We used numerical modeling of hypervelocity impact to investigate the generation mechanism and the characteristics of the resulting waves up to a distance of 100–150 projectile radii. The wave signal is primarily controlled by the ratio between projectile diameter and water depth, and can be roughly classified into deep-water and shallow-water impacts. In the latter, the collapse of the crater rim results in a wave signal similar to solitary waves, which propagate and decay in agreement with shallow-water wave theory. The much more likely scenario for an asteroid impact on Earth is a relatively small body (much smaller than the water depth) striking the deep sea. In this case, the collapse of the transient crater results in a significantly different and much more complex wave signal that is characterized by strong nonlinear behavior. We found that such waves decay much more rapidly than previously assumed and cannot be treated as long waves. For this reason, the shallow-water theory is not applicable for the computation of wave propagation, and more complex models (full solution of the Boussinesq equations) are required.

INTRODUCTION

Statistically, the most likely scenario for a meteorite impact on Earth is a relatively small body striking an ocean basin (Hills et al. 1994; Ward and Asphaug 2000). This is primarily due to the fact that oceans cover two-thirds of the Earth's surface, but also because collisions with smaller-sized objects occur on a much shorter time scale than impact events whose environmental consequences influence the entire planet. Impacts with global catastrophic effects have been found to occur very rarely throughout the history of the Earth, with a statistical flux of only ~100 million years (Chapman and Morrison 1994). The most recent of such global catastrophes was the Chicxulub event, which is now widely accepted as the incident that ended the Cretaceous period 65 Ma ago (Smit et al. 1996).

The smaller the size of the impacting body, the higher the rate of fall. However, the estimated minimum size of an asteroid that can penetrate the Earth's atmosphere is controversial, ranging between 50–200 m (Chyba et al. 1993; Bland and Artemieva 2003), depending on its composition (iron or stone) and specific material properties. Smaller objects explode and scatter during their passage through the atmosphere, raining down as fragments with relatively low velocities (Chyba et al. 1993; Artemieva and Shuvalov 2001). Statistically, asteroids 200–300 m in diameter hit the Earth approximately every 3000–4000 years (Ward and Asphaug 2000). However, more recent studies of falls in the same size range predict a rate of ~1 every 50,000–60,000 years (Bland and Artemieva 2003).

An impact event in a marine environment differs in several respects from the strike of an asteroid on land due to the water masses involved in the cratering process. Ormö and Lindström (2000) showed that there are unique geological features of impact craters generated at the ocean bottom. To form such craters, the impactor must penetrate through the water column and modify the solid strata underneath. However, if the impactor size is much smaller than the water depth, most of the energy of the impactor is dissipated within the water column, and only minor or no distinct structural modifications, such as craters, are left behind in the ocean bottom. Another important difference between continental and oceanic impacts is the vaporization of water expanding as a vapor cloud in the upper atmosphere. Earth's climate and atmospheric circulation may be severely perturbed by the injection of large amounts of vapor (e.g., Pierazzo 2005).

The most obvious consequence of oceanic impacts is the generation of water waves; the actual hazards for surrounding coastlines and coastal communities is still controversial. The pivotal point in this discussion is whether such waves can propagate on global scales, such as the tsunami on December 26, 2004, which was caused by a submarine earthquake, or whether impact-induced waves decay much faster due to their different wave characteristics. Some studies (e.g., Hills et al. 1994; Ward and Asphaug 2000) imply that even relatively small bodies, having a high rate of fall, may pose a global threat if they hit an ocean, thereby generating tsunami waves; other studies (e.g., Melosh 2003) counter that potential danger of an impact-generated tsunami is overrated. Melosh (2003) refers to studies by Van Dorn et al. (1968), who showed through explosion experiments in shallow water that a large fraction of wave energy is dissipated by wave breaking (induced near the continental shelf) and the significant influence of bottom friction while propagating/breaking on the continental shelf. This argument is supported by a recent numerical study of Korycansky and Lynett (2005). They used a monochromatic wave, representing the impact-induced wave signal to demonstrate how this wave shoals along the continental slope, finally starting to break near the continental shelf, and that the wave energy is effectively dissipated by breaking and bottom friction. Ward and Asphaug (2000) assume a linear transformation of the transient cavity in the water column and analytically compute the wave characteristics. From this theoretical approach, the authors obtained wave signals very similar to monochromatic wave trains, decaying proportional to 1/*r*, where *r* is distance from point of impact. The amplitude of the wave attenuates due to geometry spreading (circular propagation of the wave) and dispersion. However, numerical hydrocode modeling of impacts in a water column (Crawford and Mader 1998; Shuvalov and Trubestkaya 2002; Weiss et al. 2006) imply that the wave characteristics are more complex than monochromatic waves, and that the linear transformation of the transient crater may only hold for impacts into very deep water where the bottom of the ocean is not influenced by the impacting body.

In this study, we focus on the generation mechanisms that define the characteristics of the initial waves by using hydrocode modeling of oceanic impacts in different water depths and at varying impact velocities. The objectives are to constrain the parameters controlling the characteristics of the induced waves close to and at a distinct distance from the point of impact, and to investigate the fundamental differences in the characteristics of waves generated during impacts in shallow and deep water. In previous studies, the authors focus either on specific examples of marine impact craters, like the Mjølnir crater, Norway (Shuvalov et al. 2002), the Lockne crater, Sweden (Shuvalov et al. 2005), or the Eltanin structure in the Southern Ocean (Artemieva and Shuvalov 2002; Shuvalov and Trubestkaya 2002; Wünnemann and Lange 2002; Mader 1998), or they only account for the decay of the wave amplitude and the propagation velocity of the generated waves (Gisler et al. 2004). The simplified assumptions for the characteristics of impact-induced tsunami-like waves in previous studies of propagation and run-up of the waves may not reflect the natural conditions well enough. The typical characteristics of impact-induced waves are not yet thoroughly determined (Korycansky and Lynett 2005).

Cratering Mechanics and Wave Generation

The mechanics of oceanic impacts depend on the kinetic energy of the impacting body relative to the depth of the water column. A variety of values for important control parameters, such as the impact velocity, size, and mass of the projectile and the water depth, have been examined both by numerical modeling (e.g., O'Keefe and Ahrens, 1982; Crawford and Mader 1998; Wünnemann and Lange 2002; Shuvalov and Trubestkaya 2002) and in laboratory experiments (Gault and Sonett 1982). Assuming a simplified stony composition of the impactor (density $\rho = 2700$ kg/m^3), normal incidence (vertical impact), and the average impact velocity on Earth of $v_i \approx 18$ km/s (O'Keefe and Ahrens 1994), the cratering process depends only on the ratio $\gamma = d/H$, where d is the projectile diameter and H the water depth. For very small γ ratios ($\gamma < 0.1$), the projectile does not penetrate the water column. The ocean bottom is only affected by shock waves that are transmitted from the water into the pelagic strata (Artemieva and Shuvalov 2002) or by subsequent strong water currents (Wünnemann and Lange 2002), but there is no underwater crater formed in the seafloor. These impacts are called deep water impacts (DWIs). Conversely, if $\gamma > 1$, the water layer does not affect the cratering process significantly; these impacts are called shallow water impacts (SWIs). However, the final crater morphology may still differ from crater structures on land (Shuvalov and Trubestkaya 2002; Ormö and Lindström 2000). In between these two extreme cases ($0.1 < \gamma < 1$), the water column has a significant influence on crater formation (Shuvalov and Trubestkaya 2002; Weiss et al. 2006). The transition from DWI to SWI is gradual, and the definition by the γ ratio has to be considered as a broad classification. Independent of the γ ratio, water waves are generated in all cases; this study is aiming at a specification of wave characteristics as a function of water depth.

Figure 1 shows a snapshot series of a DWI (Fig. 1VIa) and an SWI (1VIb). Two mechanisms are responsible for the generation of waves (Weiss et al. 2006). First, during excavation of the crater in the ocean, water is ejected, forming an almost vertical standing ejecta cone that collapses and plunges into the water surface (Figs. 1IIa and 1IIb). The collapse of the ejecta curtain causes a water wave of large amplitude; these waves are called rim waves (RWs). In the

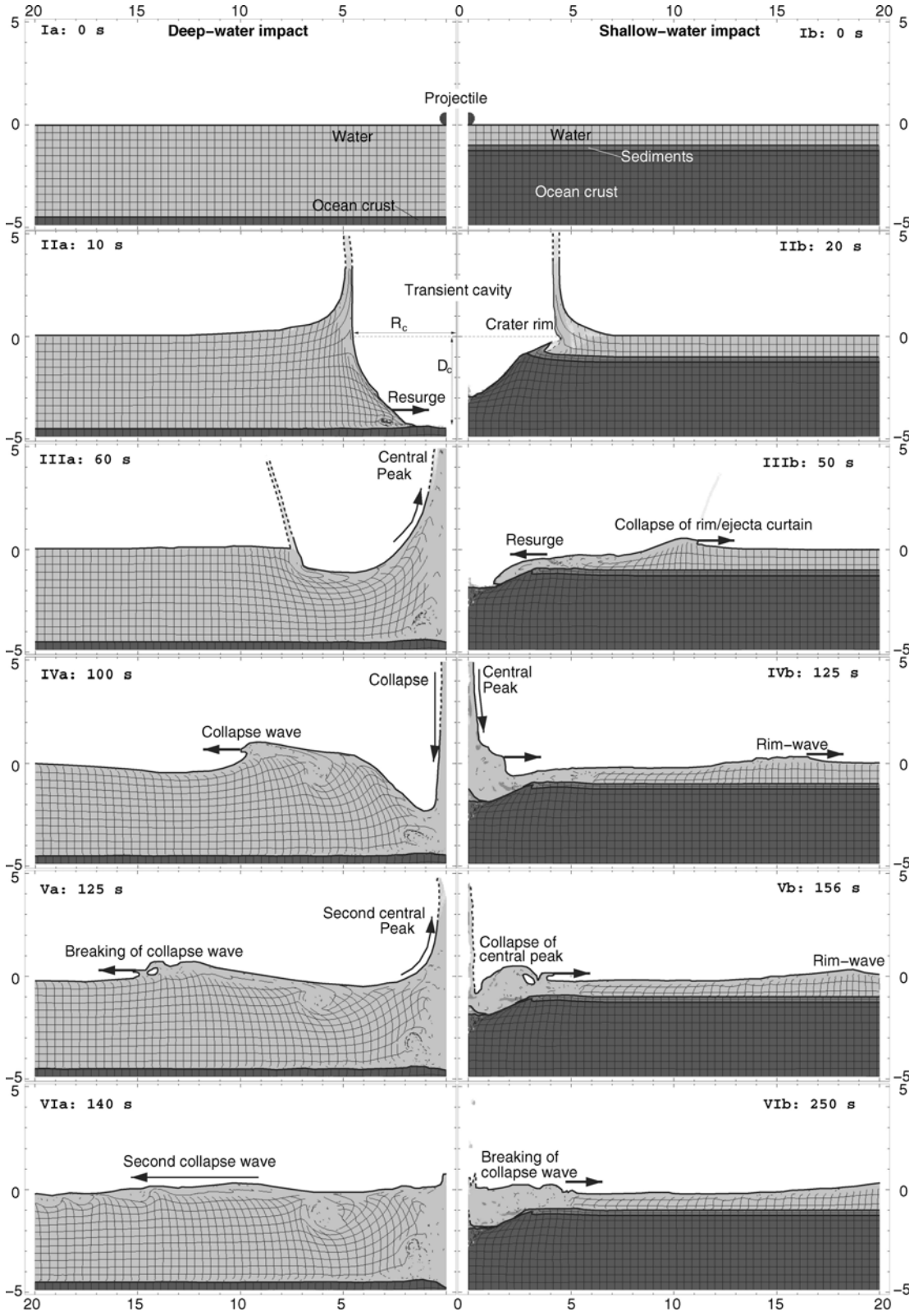

Fig. 1. Snapshot series of a deep water (left column) and a shallow water (right column) impact with $\gamma = 0.22$ and $\gamma = 0.6$. Light gray indicates the water column, medium gray a thin layer (250 m) of water-saturated sediments (only present in the SWI), and dark gray the basement. The overlaid grid depicts the deformation. In regions where mixing and turbulent flows occur no grid is plotted. R_c and D_c mark the approximate radius and depth of the transient crater.

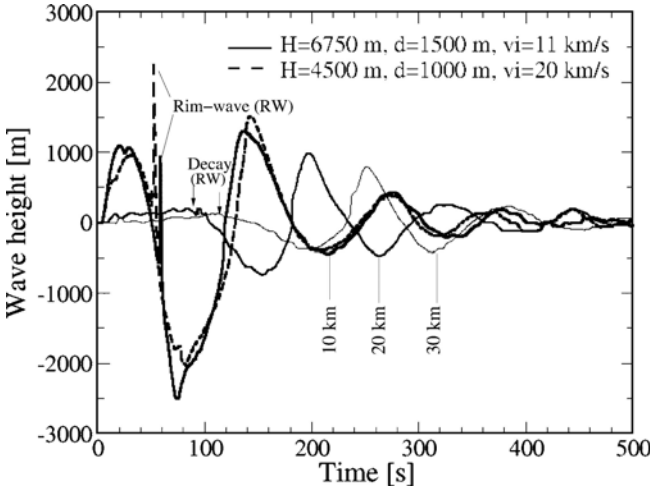

Fig. 2. Time series of wave amplitude at 10, 20, and 30 km distance from point of impact. The impact velocities v_i, the projectile diameter d, and the water depth H were varied in such a way that impact energy and the γ ratio are the same in both runs. Note the strong attenuation of the rim-wave.

case of a DWI, this wave decays almost immediately (see Fig. 2) and can be neglected for the distant wave signal. For SWIs, the RWs play an important role. Second, independent of the ratio between the water depth and the projectile diameter, the impact displaces a quantity of water resulting in the formation of a "transient" cavity in the water layer. This cavity is not stable and eventually collapses. The crater is filled by the centripetal inflow of water from the adjacent ocean. A wave trough travels away from the sites of the disturbance. The water, rushing back into the cavity, piles up to a central peak (Figs. 1IIIa and 1IIIb) that subsequently collapses (Figs. 1IVa and 1IVb), generating a wave called a collapse wave (CW). The same sequence is repeated (oscillations; Figs. 1Va and 1Vb) until the energy is dissipated and the water layer returns to its pre-impact level. The generated wave pattern can be described by concentric ring waves propagating away from the point of impact.

Collapse waves are the dominating waves of a DWI. In the case of an SWI, their generation is strongly affected by water depth, which is the controlling parameter for the velocity of the inflow. Furthermore, the juxtaposition of ongoing inflow and the generation of subsequent collapse waves result in dissipation of the primary wave signal close to the point of impact; both processes occur in the crater cavity. For large γ ratios (shallow water depth compared to the size of the projectile), the rim of the crater in the seafloor (Fig. 1IIb) can reach above the pre-impact water level and therefore may prevent water from directly flowing into the cavity. In these cases, water erodes deep channels into the crater rim and may enter the crater slowly and long after the impact event. However, in such a case, the backstream of the water is not effective or rapid enough to generate CWs. Resurge channels (gullies) were first observed at the Lockne crater in Sweden (Ormö and Miyamoto 2002; Lindström et al. 1996). However, numerical modeling and facies analysis of sediments indicate that the γ ratio was about unity at Lockne (Ormö et al. 2002), which makes it impossible that the rim could have reached above the pre-impact water level.

Numerical Model

Numerical modeling of hypervelocity impact has been used to simulate the various processes that accompany an asteroid or comet strike on land or in the ocean (e.g., Roddy et al. 1987; O'Keefe and Ahrens 1999; Pierazzo and Melosh 1999; Ivanov and Artemieva 2002; Collins and Wünnemann 2005). This study focuses on the generation mechanism of waves, and we did not attach much importance to the early stages of crater formation (contact and compression stage, excavation stage; see e.g., Gault et al. 1968; Melosh 1989; Turtle et al. 2005) with regards to the accuracy of our model. The crater collapse and the flap of the ejecta curtain are the driving mechanisms for the release of waves into the ocean and are therefore the processes our numerical models are aiming at. We used the 2-D iSALE hydrocode (Wünnemann et al. 2006), which has been used in numerous modeling studies of crater formation before (Wünnemann and Ivanov 2003; Wünnemann et al. 2005; Collins and Wünnemann 2005; Goldin et al. 2006). This code is well tested and validated against other numerical models and experimental studies.

Due to the 2-D cylindrical geometry of our model, we can only simulate vertical impacts into a layered target that is composed of the following units: 1) the water column and the oceanic crust, which consists of 2) an upper layer 250 m thick of relatively weak material mimicking water-saturated sediments, (only in SWI-calculations present), and 3) a lower part of solid hard rock. The exact composition, material properties, dimensions, and grid resolution are summarized in Table 1. However, the material properties of the seafloor are not very important because they presumably have minor or no influence on the wave-generation mechanism. The material-specific properties are described by an equation of state (EOS) and a constitutive model defining the resistance of the material against elasto-plastic deformation (strength). For the water layer we assume inviscous material properties. The material-strength model used in the seafloor and in the projectile is described in detail in Collins et al. (2004). For the calculation of thermodynamic material behavior, we used the analytic EOS (Thompson and Lauson 1972).

The grid resolution is given in Table 1. Note that the spatial increment dx varies between an inner high-resolution zone (dx = 25–100 m) and an outer extended zone (dx = 100–1000 m). After careful testing, we can rule out the possibility that changes in dx affect the resulting wave characteristics.

Effective Parameters

A fundamental assumption of our study is that the induced wave signal is invariant to the absolute thickness of the water column and projectile size, respectively. Therefore we varied only the γ ratio = *d/H*. This assumption may not hold for arbitrary combinations of *H* and *d* due to the effect of gravity in proportion to the real water depth. But for a reasonable range of water depths of the deep sea (*H* = 1000–5000), we presume that this effect is negligible and that, for instance, the impact of a 500 m projectile into a 5000 m deep ocean is similar to a 200 m impactor striking 2000 m deep sea in terms of the generated wave-forms and characteristics.

We also assume that impact velocity does not affect the generated wave signal. To test this assumption, we varied impact velocity v_i, projectile diameter *d*, and water depth *H* in such a way that the impact energy and the γ ratio were kept the same. We used $v_i = 11$ km/s, which is close to the escape velocity of the Earth, and $v_i = 20$ km/s as a reasonable range for the impact velocity. The resulting time series of wave amplitudes for the two different runs are very similar (Fig. 2). Small variations are due to slight differences in depth of the transient cavity in water. Higher impact velocities cause higher shock amplitudes resulting in a larger amount of vaporized water and thus an enlargement of the transient cavity. Furthermore, the penetration depth relative to the projectile size depends on the impact velocity, which may also cause a slightly deeper transient cavity.

Overall, we assume that the effect of impact velocity is negligible and that the characteristics of the induced waves (wave length, amplitude, decay behavior) primarily depends on the γ ratio = *d/H*.

Wave Characteristic as a Function of γ

In our numerical models, we varied γ between 0.08–1.0. To describe the properties of the generated waves, we measured the surface profile at different times ($A = f(r)|_t$), the wave elevation at defined gauge points as a function of time ($A = f(t)|_r$), and the horizontal (radial) component of the particle velocity (*v*) along vertical profiles at certain distances and points in time ($v = f(y))|_{t,r}$), where *A* is the wave amplitude, *r* is the distance from point of impact, *y* is the vertical coordinate (position in the water column), and *t* is time.

Waveforms

Figure 3 shows examples of surface profiles $A = f(r)|_t$ for a DWI (Fig. 3a: t = 205–315 s; Fig. 3b: t = 335–415 s; Δt = 20 s) and an SWI (Fig. 3c: t = 40–290 s; Δt = 50 s). For γ = 0.15, (DWI; Figs. 3a and 3b), the RW collapses immediately after its generation and is therefore negligible. In this case we focus on the waves resulting from the collapse of the transient cavity (CW). For r < 26.5 km (105–295 s), the primary wave (first CW) is characterized by wave breaking (see also Fig. 1Va), as can be seen from the steep waveforms in Fig. 3a, which results in a rapid decay of the waves due to strong dispersion. For r > 26.5 km, the wave takes on a much more regular shape and attenuates more slowly. The transition between the different decay regimes can be observed in all DWI models and occurs at an approximate distance of $r_t = 5.3 \times R_c$, and a maximum wave height of $A_{max}(r_t) = 0.6 \times \min(H, D_c)$, where R_c is the radius and D_c the depth of the transient cavity (see Fig. 1). Although our model parameters (*d, H*) span over a relatively broad range more models are required to test whether this observation is specific to all DWIs.

In Fig. 3b, wave profiles advanced in time are superimposed on Fig. 3a. Obviously, the wave amplitude of the second wavelet resulting from the collapse of a secondary central peak (second CW; see Fig 1) rises above the level of the first CW. The maximum wave amplitude is given by $A_{max}(r) = \max(A_{1CW})|_{t,r}$ for $r < r_t$, and $A_{max}(r) = \max(A_{2CW})|_{t,r}$ for $r > r_t$, where A_{1CW} and A_{2CW} are the wave amplitudes of the first and second CW, respectively. However, at larger distances, A_{1CW} is again larger than A_{2CW} due to faster attenuation of the second CW (see Fig. 4 and discussion below). The wavelengths of the first and second CW differ significantly ($\lambda_{1CW} = 22.8$ km, $\lambda_{2CW} = 14.3$ km). This, combined with the fact that the wavelength changes with

Table 1. Material parameters and numerical grid resolution.

Parameters	Values
Impactor	
Diameter/resolution	400–2000 m/16–30 cells
Impact velocity	12–22 km s^{-1}
Material/EOS	Granite, ANEOS
Water column	
Material/EOS	Water/ANEOS
Thickness/resolution	1000–5000 m/33–200 cells
Water saturated sediments (only for SWI)	
Material/EOS	Calcite/ANEOS
Thickness/resolution	0–250 m/10 cells
Strength	Cohesion; friction
Basement	
Material/EOS	Granite/ANEOS
Resolution	100 cells
Strength	Cohesion; friction
Computational mesh	
Number of cells nx × ny (radial, vertical)	975 × 550 cells
High resolution zone (nx_{HR})	600–800 cells
High resolution zone (ny_{HR})	400 cells
Spatial increment (high-resolution area)	25–100 m
Maximum spatial increment ($nx > nx_{HR}$)	100–1000 m
Maximum spatial increment ($50 < ny < ny_{HR}$)	2000 m

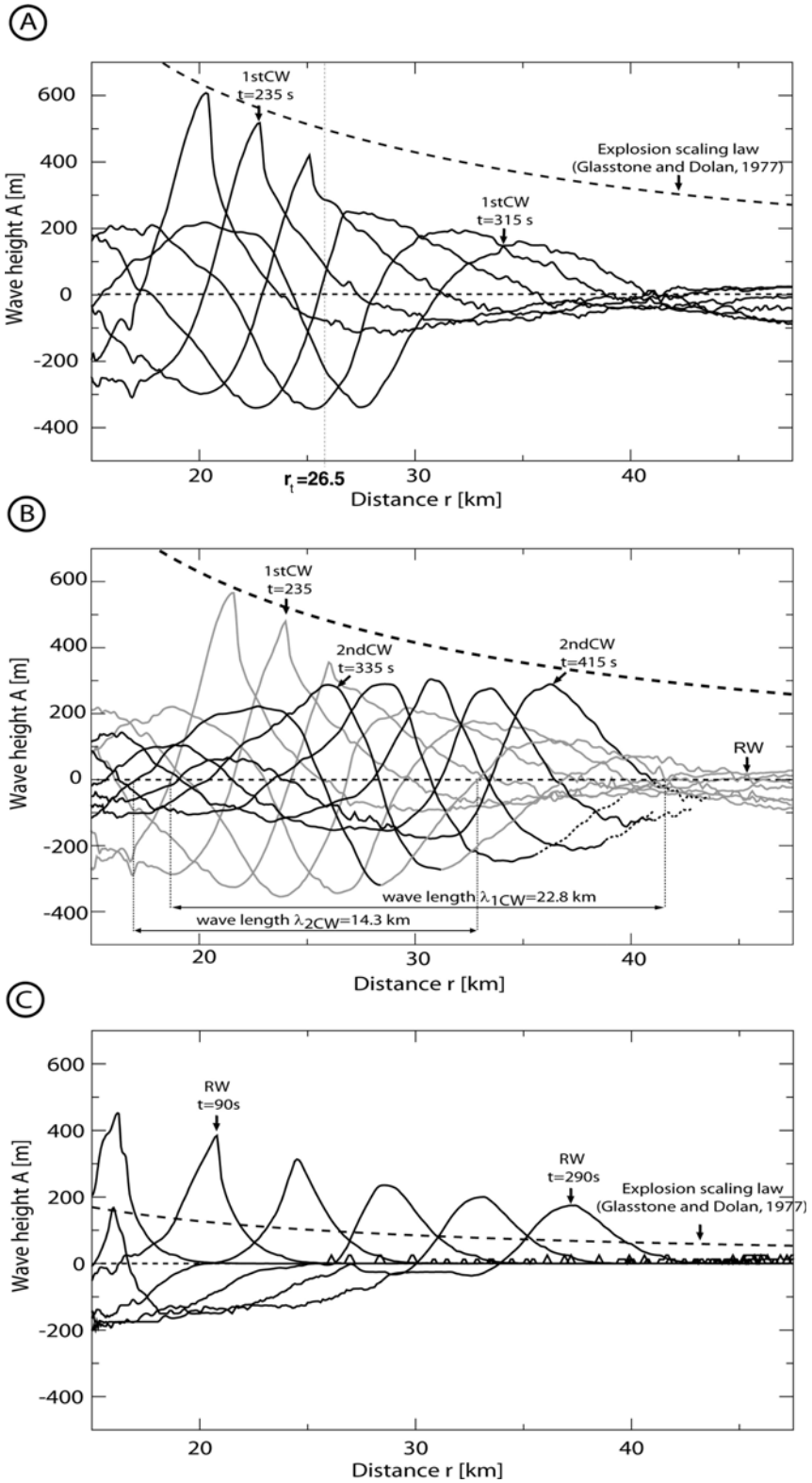

Fig. 3. Wave profiles (distance *r* versus wave amplitude *A*) for $\gamma = 0.15$ (DWI [a] and [b]) and $\gamma = 0.75$ (SWI [c]) between 15 and 47.5 km from the point of impact. a) DWI. t = 205–315 s, time between profiles Δt = 20 s, transition between different decay regimes of first CW at r_t = 26.5 km. b) DWI. t = 335–415 s (superimposed on 3a in light gray), at r_t the second CW has got a higher amplitude than first CW, the wavelength of the first CW and second CW is λ_{1CW} = 22.8 km and λ_{2CW} = 14.3 km, respectively. c) SWI. t = 40–290 s, Δt = 50 s, RW has the shape of a solitary wave. The dashed line marks the wave decay, calculated after Glasstone and Dolan (1977; Equation 4).

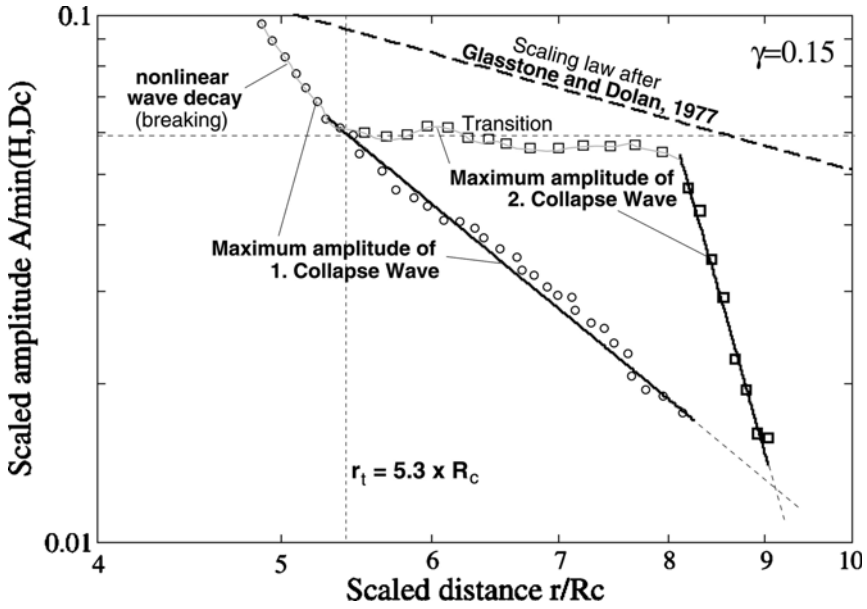

Fig. 4. Wave attenuation curves for $\gamma = 0.15$. The gray and black lines mark the maximum wave amplitude for the first CW (circles) and the second CW (squares) as a function of distance. Note the logarithmic scale of the non-dimensional units: distance r is scaled by the radius of the transient cavity in water R_c, while the wave amplitude A is normalized by the minimum of the water depth H and the depth of the transient cavity D_c. Note, that wave attenuation was analyzed only for $r > r_t$.

increasing distance, points to the dispersive character of the CW where the longer waves (first CW) travel faster than shorter waves (second CW), resulting in different attenuation rates of the first and second CW (see discussion below).

In an SWI, the wave characteristics differ significantly from those of a DWI. Figure 3c shows the waveform between 15–47.5 km for different points in time (t = 40–290 s). The γ ratio is 0.75. As shown in Fig. 1, the first wave signal of an SWI comes from the collapse of the crater rim plunging through the water surface. The RW is best described as a solitary wave that decays with increasing distance from point of impact. In the example shown, bidirectional water currents inhibit the generation of a pronounced CW (see previous description of Fig. 1) and our models have shown that secondary wave signals (CWs) are generally negligible for $\gamma \geq 0.75$.

Wave Attenuation

The attenuation of impact-induced waves is complex and varies between different wave types, as seen in the surface profiles in Fig. 3. For long waves where no or very weak dispersion occurs, the attenuation factor can be derived from linear wave theory and is $\propto 1/\sqrt{r}$ due to the radial spreading of the waves. Dispersive waves decay much faster in proportion to $1/r^q$, where $0.5 \leq q \leq 1$ (Ward and Asphaug 2000; Weiss et al. 2006). Attenuation coefficients q larger than 1 clearly point to nonlinear effects such as dissipation via turbulence, wave breaking, and wave group dynamics. Solitary waves are subject to a different decay behavior; the radial spread results in a reduction of the amplitude in proportion to $q = 2/3$ (Mai 1989).

To determine the attenuation of the generated waves in our models, we used time series in increasing distance to the point of impact. We analyzed the rim wave and the first and second collapse waves separately to study the relative importance of the different wave categories for different types of impacts. An example (γ = 0.15) of wave attenuation is shown in Fig. 4. The bold, gray, and black lines depict the maximum amplitude A_{max} as a function of distance. Due to highly nonlinear effects for distances smaller than r_t (such as wave breaking) (Fig. 3a and Fig. 1Va), we analyzed the attenuation of the waves only for $r > r_t$, where the amplitude of the second CW (squares) becomes bigger than the one of the first CW (circles). The two separate branches of the attenuation curves, one for the first CW (the lower curve marked by circles) and one for the second CW (upper curve marked by squares) illustrate the different decay behavior. For both branches, we fit a function in proportion to $1/r^q$ and determined the attenuation factor q. We interpolated only over a range where we could make sure that wave breaking did not affect the decay of the waves and the waveforms (see Fig. 3) have taken on a relatively smooth shape. Note that in the shown example, the second CW attenuates faster than the first CW, and thus $A_{max} = \max(A_{1CW})$ for $r > 9 \times R_c$. The results of all models in terms of the attenuation factor q are listed in Table 2. In Fig. 5, the factor q (determined for $r > r_t$) is plotted versus γ to demonstrate that CWs are reduced faster in deeper water (smaller γ ratios) than in shallow water (larger γ ratios). For $\gamma \geq 0.75$, no CW occurs. The RW decays much more slowly, ranging between q = 1.38 for $\gamma = 0.6$ and q = 0.72 for $\gamma = 1.0$.

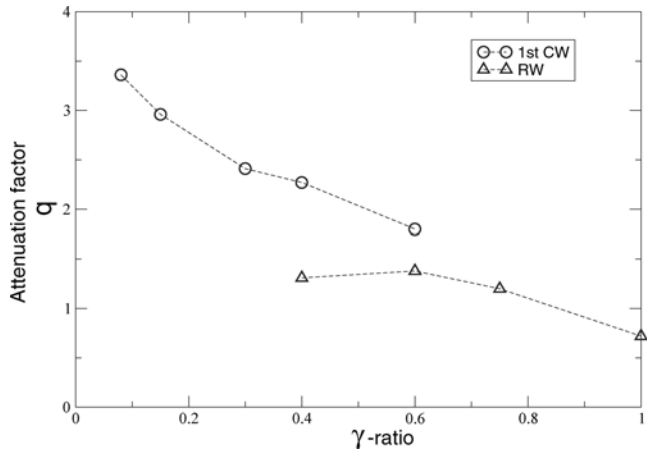

Fig. 5. Attenuation factor q of the first CW (circles) and the RW (triangles) as a function of γ ratio for $r > r_t$.

Our attenuation factors are generally in good agreement with the results of previous modeling studies on oceanic impacts (Gisler et al. 2004; Shuvalov and Trubestkaya 2002). However, in these studies, only the decay of the first wave (first CW) was determined, which has to be compared with the minimum attenuation factor for a specific γ ratio in our models. For almost all γ ratios, we found that either the RW or the first CW defines the maximum amplitude at larger distances ($r > 9 \times R_c$) from the point of impact. The only exception occurs for γ = 0.08, where the second CW generates the highest amplitude.

It has to be taken into consideration that the very strong damping of CWs in DWI may be artificially enhanced due to under-resolution in hydrocode modeling of turbulent processes and wave breaking. However, tests have shown that higher resolutions in the near field, close to the impact where nonlinear effects are dominant, do not significantly influence the resulting wave profiles at larger distances. We also tested whether any extra dissipation is introduced numerically that may affect (enhance) the attenuation behavior. For this purpose, we modeled wave propagation resulting from the collapse of a bowl-shaped cavity of moderate depth (d = 200, R_c = 1200 m). We found an excellent agreement with the theory, namely, that the wave height decays in proportion to *1/r*. The only reasonable explanation for the much higher attenuation factors of the waves in the impact models is some enhanced dissipation of wave energy driven by nonlinear effects, such as wave group dynamics (wave-wave interaction), the steepness of the waves and/or a complex velocity field (turbulent processes) underneath the wave (see the next section). Enhanced dispersion should result in a significant increase of wavelength or period, which does not seem to be the case (wavelength changes only slightly) in our models.

Vertical Profiles of the Horizontal Velocity Field

The basic idea of wave propagation is that energy is transmitted from one water particle to the adjacent ones, which are then forced to move along orbital pathways as the wave crest and trough pass at the surface. In a classic tsunami wave (generated by an earthquake, for instance), the orbits always reach down to the seafloor due to their long wavelength λ (λ >> H). Therefore such waves are considered to be long or shallow-water waves; no considerable change of v can be observed with depth. In our models, the vertical profiles of the radial velocity component are different for RWs (SWI) and CWs (DWI) as shown in Fig. 6. For an SWI, (γ = 0.75) the velocity profile of the RW does not considerably change with depth. The mean value agrees well with the velocity, which can be determined from the shallow-water theory:

$$v = A\sqrt{\frac{g}{H}} \quad (1)$$

In contrast, the velocity of the CW shows a steep decline in depth and goes down to almost zero at about 0.5 × H. In deep water, the CW does not reach down to the ocean bottom and therefore decays faster than classical (long) shallow-water waves. This is an important distinction between classical tsunamis and impact-induced waves in deep water.

Table 2. Attenuation factor q for the rim-wave (RW) and the first collapse-wave (first CW) and different γ ratios.

γ ratio	RW	First CW
0.08	–	3.36
0.15	–	2.96
0.3	–	2.41
0.4	1.31	2.27
0.6	1.38	1.8
0.75	1.20	–
1.0	0.72	–

DISCUSSION

The detailed analysis of the impact-induced waves in the vicinity of the impact site reveals a complex wave characteristic that significantly depends on the water depth—projectile diameter ratio γ. Our work comprises only impacts with normal incidence; the characteristics of generated waves may be even more complex for oblique impacts. However, Shuvalov et al. (2005) has demonstrated that only minor changes with respect to the circular symmetry of the generated waves occur in the far field, and we assume that for impact angles ≥45° the effect of obliquity is negligible. This assumption will be tested more thoroughly in future work.

The most complex wave signal is generated for intermediate γ ratios (0.4 ≤ γ ≤ 0.6), because all wave types RWs and CWs are released by the impact. For γ's larger than ~0.6, only an RW is generated; for γ < 0.4, the RW is directly dissipated due to the collapse of the transient cavity in the water, and the wave signal consists only of CWs.

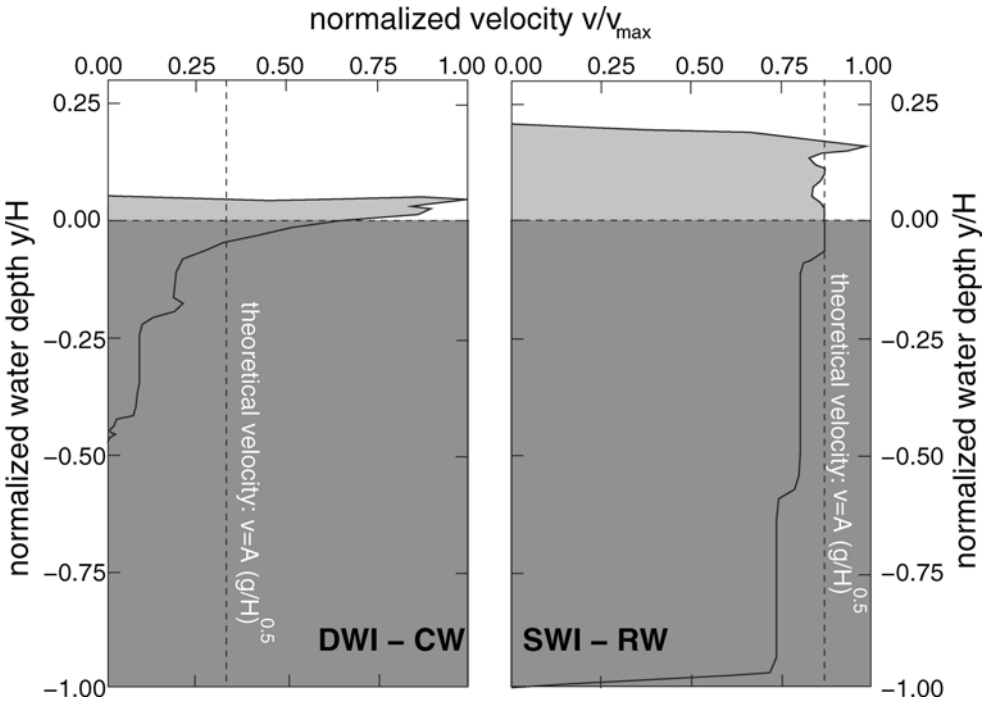

Fig. 6. Vertical profile through the water column of the radial velocity component for the CW (r = 19.6 km, t = 300 s) at a DWI (γ = 0.15) and for the RW (r = 38 km, t = 300 s) at a SWI. The dashed lines mark the theoretically determined velocity of a shallow-water wave.

The RW is best described as a solitary wave that decays with distance from the point of impact. In our models, the attenuation factor q ranges between 1.38 and 0.72, depending on the γ ratio. This is a slightly bigger value than the theoretically derived damping ratio of two-thirds (e.g., Mai 1989). We presume that once the wave loses direct contact to the ocean bottom, the wave decays faster. This assumption is supported by the fact that profiles of the radial velocity change slightly with depth for smaller γ ratios but are almost constant for larger γ values. Waves with constant velocity profiles through the water column can be treated as shallow-water waves where the wavelength is significantly larger than the water depth. Therefore, we conclude that the propagation of RWs can be computed by classical shallow-water theory (e.g., Ward and Asphaug 2003; Matsuii et al. 2002; Weiss et al. 2006).

In contrast to the solitary RW, CWs always consist of a wave crest and trough. The attenuation factors of the CWs are much higher and vary between 1.80 and 3.36. These values are in the range of the attenuation factors proposed in earlier numerical (Mader 1998; Gisler et al. 2004) and analytical models (Ward and Asphaug 2000). However, in these studies, the authors describe the wave decay of A_{max} and do not distinguish between different wave types.

The decreasing trend of q in Fig. 5 for the CW can be ascribed to the fact that the water column is involved to greater depth in the collapse of the transient crater for larger γ's. Thus, the smaller the γ ratio, the faster the radial velocity v decays with depth and the more rapidly the wave amplitude attenuates with distance. We therefore conclude that CWs cannot be treated as long waves; the attenuation factors would be underestimated. However, at distances further from the point of impact, the wave characteristics may become more linear due to wave damping and eventually evolve into shallow-water waves. This corresponds to the formula proposed by Glasstone and Dolan (1977) describing the wave attenuation A_{max} in proportion to $1/r$:

$$A_{max}(r) = 45(Y)^{1/4}\frac{\min(H, D_c)}{r} \quad (2)$$

This equation is based on empirical investigations of the Baker nuclear explosion in the 60 m deep lagoon on Bikini Atoll (Glasstone and Dolan 1977). Y is the kinetic energy of the impactor in kt TNT (in the experiment, an energy of 20 kt TNT was released). Shuvalolv and Trubestkaya (2002) found a relatively good agreement between numerical modeling results and Equation 2 for the wave decay of a DWI, but not for an SWI. Our modeling results indicate that Equation 2 underestimates the wave amplitude of the RW at SWI (Fig. 3c). For DWIs, the predicted wave amplitude according to Equation 2 is in reasonable agreement with the modeling results for the all-time maximum amplitude A_{max} (see dashed line in Figs. 3a and 3b). However the attenuation factors for each wave type (first CW, second CW, RW) indicate higher damping rates than in Equation 2. More models, especially for very small γ ratios, are required to investigate the decay behavior of A_{max}, particularly in the far field.

CONCLUSION AND SUMMARY

Detailed analysis of impact-generated large water waves through numerical modeling demonstrates the complex characteristics of the induced waves. The wave signal is primarily controlled by the ratio of the projectile diameter and the water depth $\gamma = d/H$. The impact velocity and, presumably, the impact angle are negligible. The wave characteristics depend on the generation mechanism: rim-waves originate from the collapse of the ejecta curtain plunging through the water surface; collapse-waves evolve from the collapse of the transient cavity in the water column. Rim-waves occur only in relatively shallow water (SWI; $\gamma > 0.4$), while collapse-waves are the dominating mechanism for impacts in deep water (DWI; $\gamma < 0.4$). The characteristics of both wave types differ significantly. Rim-waves are best described as solitary waves decaying at a relatively moderate rate in proportion to $(1/r)^q$, with q = 1.38–0.72 for increasing γ. Collapse-waves have a trough and a peak, and decay much more rapidly (q = 1.8–3.36).

As a DWI is the most likely scenario for future meteorite impacts on Earth, the generation of collapse-waves has to be taken into account when assessing the potential hazards of such an event. Our results show that these waves decay much more rapidly than previously assumed in wave propagation models that estimate the consequences for coastal areas far from the point of impact (Ward and Asphaug 2000, 2003; Weiss et al. 2006). However, our models characterize the wave behavior only in a relatively small area around the point of impact, and we cannot rule out that the generated waves eventually evolve into typical shallow-water waves with much smaller attenuation rates. Nevertheless, our models show that shallow-water wave theory is not applicable, at least up to 150 projectile radii from the point of impact. Due to the simplified assumption that the generated waves can be described as long-waves, we presume that the arriving wave amplitudes at the surrounding coastlines were overestimated in previous studies. For a more realistic assessment of the hazards of impact tsunamis, further work is required to investigate how wave characteristics may change with distance, for instance, by using a model where the full (incompressible) Boussinesq equations are solved.

Acknowledgments—We are grateful to D. G. Korycanski and V. V. Shuvalov for constructive and insightful reviews that improved the final version of the manuscript. This work was supported by DFG grant WU 355/5–1.

Editorial Handling—Dr. Jens Ormö

REFERENCES

Artemieva N. A. and Shuvalov V. V. 2001. Motion of a fragmented meteoroid through the planetary atmosphere. *Journal of Geophysical Research* 106:3297–3310.

Artemieva N. A. and Shuvalov V. V. 2002. Shock metamorphism on the ocean floor (numerical simulations). *Deep-Sea Research II* 49:959–968.

Bland P. A. and Artemieva N. A. 2003. Efficient disruption of small asteroids by Earth's atmosphere. *Nature* 424:288–291.

Chapman C. R. and Morrison D. 1994. Impacts on Earth by asteroids and comets: Assessing the hazard. *Nature* 367:33–40.

Chyba C. F., Thomas P. J., and Zahnle K. J. 1993. The 1908 Tunguska explosion: Atmospheric disruption of a stony asteroid. *Nature* 361:44–44.

Collins G. S. and Wünnemann K. 2005. How big was the Chesapeake Bay impact? Insight from numerical modelling. *Geology* 33: 925–928.

Collins G. S., Melosh H. J., and Ivanov B. A. 2004. Modeling damage and deformation in impact simulations. *Meteoritics & Planetary Science* 39:217–231.

Crawford D. A. and Mader C. 1998. Modeling asteroid impact and tsunami. *Science of Tsunami Hazard* 16:21–30.

Gault D. E. and Sonett Ch. P. 1982. Laboratory simulation of pelagic asteroidal impact: Atmospheric injection, benthic topography, and the surface wave radiation field. In *Geological implications of impacts of large asteroids and comets on the Earth*, edited by Silver L. T. and Schultz P. H. GSA Special Paper #190. Boulder, Colorado: Geological Society of America. pp. 69–92.

Gault D. E., Quaide W. L., and Oberbeck V. R. 1968. Impact cratering mechanics and structures. In *Shock metamorphism of natural materials*, edited by French B. M. and Short N. M. Baltimore, Maryland: Mono Book Co. pp. 87–99.

Gisler G. R., Weaver R. P., Mader C. L., and Gittings M. L. 2004. Two- and three-dimensional asteroid impact simulations. *Computing in Science and Engineering* 4:46–55.

Glasstone S. and Dolan P. J. 1977. *The effects of nuclear weapons*. Washington, D.C.: U.S. Government Printing Office. 653 p.

Goldin T. J., Wünnemann K., Melosh H. J., and Collins G. S 2006. Hydrocode modeling of the Sierra Madera impact structure, *Meteoritics & Planetary Science* 41:1947–1958.

Hills J. G., Nemchinov I. V., Popov S. P., and Teterev A. V. 1994. Tsunami generated by small asteroid impact. In *Hazards from comets and asteroids*, edited by Gehrels T. Tucson, Arizona: The University of Arizona Press. pp. 779–789.

Ivanov B. A. and Artemieva N. A. 2002. Numerical modelling of the formation of large impact craters. In *Catastrophic events and mass extinctions: Impacts and beyond*, edited by Koeberl C. and MacLeod K. G. GSA Special Paper #356. Boulder, Colorado: Geological Society of America. pp. 619–629.

Korycansky D. G. and Lynett P. J. 2005. Offshore breaking of impact tsunami: The Van Dorn effect revisited. *Geophysical Research Letters* 32, doi:10.1029/2004GL021918, 2005.

Lindström M., Sturkell E. F. F., Törnberg R., and Ormö J. 1996. The marine impact crater at Lockne, central Sweden. *Geologiska Foremingens Stockholm Forhandlingar* 118:193–206.

Mader C. L. 1998. Modeling the Eltanin asteroid tsunami. *Science of Tsunami Hazards* 16:17–21.

Matsuii T., Imamura E., Tajika E., Nakano Y., and Fujisawa Y. 2002. Generation and propagation of a tsunami from the Cretaceous-Tertiary impact event. In *Catastrophic events and mass extinctions: Impacts and beyond*, edited by Koeberl C. and MacLeod K. G. GSA Special Paper #356. Boulder, Colorado: Geological Society of America. pp. 69–77.

Mei C. C. 1989. *The applied dynamics of ocean surface waves*. Singapore: World Scientific Publishing Co. 740 p.

Melosh H. J. 1989. Impact cratering—A geological process. New York: Oxford University Press. 245 p.

Melosh H. J. 2003. Impact-generated tsunamis: An overrated hazard (abstract #2013). 34th Lunar and Planetary Science Conference. CD-ROM.

O'Keefe J. D. and Ahrens T. J. 1982. The interaction of the Cretaceous/Tertiary extinction bolide with the atmosphere, ocean, and solid Earth. In *Geological implications of impacts of large asteroids and comets on the Earth*, edited by Silver L. T. and Schultz P. H. GSA Special Paper #190. Boulder, Colorado: Geological Society of America. pp. 102–120.

O'Keefe J. D. and Ahrens T. J. 1994. Impact-induced melting on planetary surfaces. In *Large meteorite impacts and planetary evolution*, edited by Dressler B. O., Grieve R. A. F., and Sharpton V. L. GSA Special Paper #293. Boulder, Colorado: Geological Society of America. pp. 103–109.

O'Keefe J. D. and Ahrens T. J. 1999. Complex craters: Relationship of stratigraphy and rings to impact conditions. *Journal of Geophysical Research* 104:27,091–27,104.

Ormö J. and Lindström M. 2000. When a cosmic impact strikes the sea bed. *Geological Magazine* 137:67–80.

Ormö J., Shuvalov V. V., and Lindström M. 2002. Numerical modeling for target water depth estimations of marine target impact craters. *Journal of Geophysical Research* 107, doi:10.1029/2002JE001865.

Ormö J. and Miyamoto H. 2002. Computer modeling of the water resurge at a marine impact: the Lockne crater, Sweden. *Deep-Sea Research II* 49:983–994.

Pierazzo E. and Melosh H. J. 1999. Hydrocode modeling of Chicxulub as an oblique impact event. *Earth and Planetary Science Letters* 165:163–176.

Pierazzo E. 2005. Assessing atmospheric water injection from oceanic impacts (abstract #1987). 36th Lunar and Planetary Science Conference. CD-ROM.

Roddy D. J., Schuster S. H., Rosenblatt M., Grant L. B., Hassig P. J., and Kreyenhagen K. N. 1987. Computer simulation of large asteroid impacts into ocean and continents—Preliminary results on atmospheric, cratering, and ejecta dynamics. *International Journal of Impact Engineering* 5:525–541.

Shuvalov V. V., Dypvik H., and Tsikalas F. 2002. Numerical simulations of the Mjølnir impact crater. *Journal of Geophysical Research* 107, doi:10.1029/2001JE001698.

Shuvalov V. V. and Trubestkaya I. A. 2002. Numerical modeling of marine impacts. *Solar System Research* 36:417–430.

Shuvalov V. V., Ormö J., and Lindström M. 2005. Hydrocode Simulation of the Lockne marine target impact event. In *Impact tectonics*, edited by Koeberl C. and Henkel H. New York: Springer. pp. 405–422.

Smit, J., Th. B. Roep, Alvarez W., Montanari A., Claeys P., Grajales-Nishimura J. M., and Bermundez J. 1996. Coarse-grained, clastic sandstone complex at the K/T boundary around the Gulf of Mexico: Deposition by tsunami waves induced by the Chicxulub impact? In *The Cretaceous-Tertiary event and other catastrophes in Earth history*, edited by Ryder G., Fastovski D., and Gartner S. GSA Special Paper #332. Boulder, Colorado: Geological Society of America. pp.151–182.

Thompson S. L. and Lauson H. S. 1972. Improvements in the Chart D radiation-hydrodynamic code 3: Revised analytic equation of state. Report SC-RR-71 0714. Albuquerque, New Mexico: Sandia Laboratories. 119 p.

Turtle E. P., Pierazzo E., Collins G. S., Osinski G. R., Melosh H. J., Morgan J. V., and Reimold W. U. 2005. Impact structures: What does crater diameter mean? In *Large meteorite impacts III*, edited by Kenkmann T., Hörz F., and Deutsch A. GSA Special Paper #384. Boulder, Colorado: Geological Society of America. pp. 1–24.

Van Dorn W. G. and Le Mehaute B. 1968. Handbook of explosion-generated water waves. Report TC-130. Pasadena, California: Tetra Tech Inc. 192 p.

Ward S. N. and Asphaug E. 2000. Asteroid impact tsunami: A probabilistic hazard assessment. *Icarus* 145:64–78

Ward S. N. and Asphaug E. 2003. Asteroid impact tsunami of 2880 March 16. *Geophysical Journal International* 153:F6–F10.

Weiss R., Wünnemann K., and Bahlburg H. 2006. Numerical modelling of generation, propagation and run-up of tsunamis caused by oceanic impacts: model strategy and technical solutions. *Geophysical Journal International* 167:77–88.

Wünnemann K. and Lange M. A. 2002. Numerical modelling of impact induced modifications of the deep-sea floor. *Deep-Sea Research II* 49:969–981.

Wünnemann K. and Ivanov B. A. 2003. Numerical modelling of impact crater depth-diameter dependence in an acoustically fluidized target. *Planetary and Space Science* 51:831–845.

Wünnemann K., Morgan J. V., and Jödicke H. 2005. Is Ries crater typical for its size? An analysis based upon old and new geophysical data and numerical modeling, In *Large meteorite impacts III*, edited by Kenkmann T., Hörz F., and Deutsch A. GSA Special Paper #384. Boulder, Colorado: Geological Society of America. pp. 67–83.

Wünnemann K., Collins G. S., and Melosh H. J. 2006. A strain-based porosity model for use in hydrocode simulations of impacts and implications for transient-crater growth in porous targets. *Icarus* 180:514–527.